Accounting for speckle-scale beam bending in classical ray tracing schemes for propagating realistic pulses in indirect drive ignition conditions

C. Ruyer,[1,2,a] ⓘD P. Loiseau,[1,2] ⓘD G. Riazuelo,[1,2] R. Riquier,[1] ⓘD A. Debayle,[1,2] ⓘD P. E. Masson-Laborde[1,2] ⓘD
and O. Morice[1]

AFFILIATIONS

[1] CEA, DAM, DIF, F-91297 Arpajon, France
[2] CEA, LMCE, Université Paris-Saclay, 91680 Bruyères-le-Châtel, France

[a] Author to whom correspondence should be addressed: charles.ruyer@cea.fr

ABSTRACT

We propose a semi-analytical modeling of smoothed laser beam deviation induced by plasma flows. Based on a Gaussian description of speckles, the model includes spatial, temporal, and polarization smoothing techniques, through fits coming from hydrodynamic simulations with a paraxial description of electromagnetic waves. This beam bending model is then incorporated into a ray tracing algorithm and carefully validated. When applied as a post-process to the propagation of the inner cone in a full-scale simulation of a National Ignition Facility (NIF) experiment, the beam bending along the path of the laser affects the refraction conditions inside the hohlraum and the energy deposition, and could explain some anomalous refraction measurements, namely, the so-called glint observed in some NIF experiments.

I. INTRODUCTION

Many experiments conducted in multi-kilojoule laser facilities, whether they concern astrophysical phenomena, high-energy-density physics,[1] or inertial confinement fusion (ICF),[2-4] bring critical insights into matter under extreme conditions. In these facilities, energetic laser beams are used to heat and compress the matter to millions of degrees and mega- to gigabar pressures. The predictability of these experiments requires a precise understanding of laser–plasma interactions, such as the mechanisms responsible for the energy deposition and those responsible for the growth of various instabilities such as stimulated Raman or Brillouin scattering,[5-8] cross-beam energy transfer,[9] two-plasmon decay,[10,11] collective scattering,[12-14] and self-focusing.[15]

Furthermore, optical smoothing techniques combining random-phase plates (RPPs) and smoothing by spectral dispersion (SSD), available at the Laser Méga Joule (LMJ) facility, the National Ignition Facility (NIF), the Laboratory for Laser Energetics (LLE), and SG-III-class lasers, improve the laser intensity profile.[16,17]

These techniques reduce the spatial coherence (through RPPs) and temporal coherence (through SSD) of the light, resulting in intensity fluctuations on the scale of a few wavelengths and lasting a few picoseconds: the so-called speckles. Polarization smoothing (PS), which consists in splitting the pulse into two uncorrelated superimposed beams with perpendicular polarizations, may also be used. Together, these smoothing techniques will in turn affect the laser–plasma interactions on macroscopic scales, such as the energy deposition region,[18,19] the scattering direction of the light wave,[20-25] and the amount of expected reflectivity.[26-29] Accounting for the hot-spot dynamics thus requires to reconcile the sub-micrometer and sub-picosecond physics of the RPP/SSD beam with the millimeter size and nanosecond duration of the experiments. In this context, a hydrodynamic description of the plasma can be coupled with an approximated Maxwell solver.[30-34] However, this formalism fails to capture self-consistently the Landau damping of acoustic waves or other kinetic effects and may turn out to be numerically unsuitable whenever multidimensional effects, solid-density physics, or radiative phenomenons arise.

In such systems, hydrodynamic codes rest on a rough description of light, such as the classical ray tracing scheme,[35–38] which, in its native form, only captures the wave refraction and basic energy deposition. Accurate description, by the ray tracing scheme, of simple light properties such as the intensity of the wave and its local spectrum, is still an active area of research.[39–42] Although great efforts have been made to improve these schemes by including back or side scattering of the light caused by wave mixing processes,[41,43] modeling of the speckle-scale physics remains largely unexplored.[44–47]

Although the flow-induced deviation may be entangled with other wave mixing processes,[25] this study addresses the beam bending of a laser beam[48–51] under the assumption that other instabilities, such as filamentation and forward/backward Brillouin/Raman scattering, are negligible. The beam bending occurs when the laser-driven density fluctuations are advected by a flow, resulting, owing to a wave-guide effect, to deflection of the electromagnetic wave from its original axis of propagation, toward the flow direction. As this effect may take place in a perfectly homogeneous plasma, the beam deflection may add up to the well-known refraction of light caused by density gradients.

In Sec. II, we first briefly recall the kinetic and fluid modeling of Ref. 52, which predicts the deflection angle of a Gaussian laser pulse, in both the transient and asymptotic regimes of the plasma density response. The model is then extended in Sec. III to the centroid deviation of a spatially (using RPP) and temporally (with SSD) incoherent laser pulse, with the effect of polarization smoothing by fits coming from three-dimensional (3D) Parax[53] simulations. Our model is incorporated into a ray tracing description of the beam propagation and compared successfully with our numerical results in Sec. IV. Then, the laser propagation under realistic indirect drive ICF plasma conditions (NIF Shot N181209 from the Hybrid B campaign[54–57]) is addressed and evidences a sensible impact of the flow-induced deviation on the light energy path and energy deposition. Our concluding remarks and perspectives are gathered in Sec. V.

International system of units (SI) units are used throughout this paper, the Boltzmann constant is dropped, temperatures are given in eV, and vectors are denoted by bold symbols.

II. BEAM BENDING OF A SPATIOTEMPORALLY INCOHERENT LASER PULSE

A. Beam bending in the transient regime

In Ref. 50, it is proved that in the small-angle limit, the transverse averaged beam wavevector $\langle \mathbf{k}_\perp \rangle_{\mathbf{k}_\perp}$ can be related to the plasma electron density fluctuations δn_e through

$$\frac{1}{k_0} \frac{d \langle \mathbf{k}_\perp \rangle_{\mathbf{k}_\perp}}{dx} \cdot \frac{\mathbf{v}_d}{|\mathbf{v}_d|} = \frac{-1}{2} \frac{n_e}{n_c} \left\langle \nabla_\perp \frac{\delta n_e}{n_e} \right\rangle_\perp, \quad (1)$$

$$\langle X \rangle_\perp = \frac{\int d\mathbf{r}_\perp X(\mathbf{r}) I(\mathbf{r})}{\int d\mathbf{r}_\perp I(\mathbf{r})}, \quad (2)$$

$$\langle X \rangle_{\mathbf{k}_\perp} = \frac{\int d\mathbf{k}_\perp X(\mathbf{k}) I(\mathbf{k})}{\int d\mathbf{k}_\perp I(\mathbf{k})}, \quad (3)$$

where we have introduced $k_0 = 2\pi/\lambda_0$, n_c, and $\mathbf{v}_d$, the main laser wavevector, critical density, and flow velocity, respectively. Moreover, $\mathbf{r}_\perp$ and $\mathbf{k}_\perp$ are the position and wavevector transverse to the main laser x direction. The transverse averages in real and Fourier space, $\langle \cdot \rangle_\perp$ and $\langle \cdot \rangle_{\mathbf{k}_\perp}$, respectively, are defined through Eqs. (2) and (3). We assume hereinafter a perfectly homogeneous plasma. The dependence of the normalized density fluctuations on time and position, $\delta n_e(t, \mathbf{r})/n_e$, will be assumed to follow the linearized hydrodynamic equations. In the plasma rest frame and after a transverse Fourier transform [defined hereinafter as $f(\omega, \mathbf{k}) = \int f(t, \mathbf{r}) e^{-i\mathbf{k}\cdot\mathbf{r}+i\omega t} d\mathbf{r}\, dt$], the relation between the density fluctuations and the laser intensity $I(\mathbf{k}) = I_0 g(\mathbf{k})$ satisfies

$$\left(\frac{\partial^2}{\partial t^2} + 2\gamma_0 |\mathbf{k}| c_s \frac{\partial}{\partial t} + c_s^2 \mathbf{k}^2 \right) \frac{\delta n_e}{n_e} = A_{|\mathbf{k}|} \frac{c_s^2 \mathbf{k}^2 I_0}{n_c v_g T_e} \frac{\alpha_k}{\alpha_f} g(\mathbf{k}) e^{i\mathbf{v}_d \cdot \mathbf{k} t}. \quad (4)$$

Here, we have introduced the sound speed $c_s = [(Z_i T_e + 3T_i)/m_i]^{1/2}$, the electron/ion mass and temperature $m_{e/i}$ and $T_{e/i}$, the normalized acoustic Landau damping rate $\gamma_0 = \nu/|k|c_s$, the laser group velocity $v_g = c\sqrt{1 - n_e/n_c}$, and the light speed in vacuum c. The ratio α_k/α_f, where

$$\alpha_k[M_0 \cos(\theta)] = \frac{-\mathscr{Z}'(\zeta_e)}{2} \frac{\sum_i \mathscr{Z}'(\zeta_i) \frac{Z_i T_e}{T_i} \frac{Z_i n_e}{n_i}}{\mathscr{Z}'(\xi_e) + \sum_i \mathscr{Z}'(\zeta_i) \frac{Z_i T_e}{T_i} \frac{Z_i n_e}{n_i}}, \quad (5)$$

$$\zeta_{e/i} = \frac{-\mathbf{k}_\perp \cdot \mathbf{v}_d}{|\mathbf{k}_\perp|} \sqrt{\frac{m_{e/i}}{2T_{e/i}}}, \quad (6)$$

$$\alpha_f[M_0 \cos(\theta)] = \frac{\kappa}{1 - M_0^2 \cos^2\theta + 2i\gamma_0 |M_0| \cos\theta}, \quad (7)$$

$$\cos(\theta) = \frac{\mathbf{k}_\perp \cdot \mathbf{v}_d}{|\mathbf{k}_\perp||\mathbf{v}_d|}, \quad (8)$$

$$\kappa = \frac{Z_i T_e}{m_i c_s^2}, \quad (9)$$

introduced in Ref. 52, is an *ad hoc* correction that ensures convergence to the kinetic asymptotic limit for highly Landau-damped plasmas. We have also introduced the Mach number $M_0 = \mathbf{v}_d/c_s$ and $\mathscr{Z}'$, the first-order derivative of the plasma dispersion function.[58] Finally, the factor A_k on the right-hand side of Eq. (4) accounts for nonlocal thermal effects on the density fluctuation amplitude[59,60] and can be written as

$$A_k(u) = \frac{1}{2} + Z_i \left(\frac{0.074}{u^2} + \frac{0.88}{u^{4/7}} + \frac{2.54}{1 + 5.5u^2} \right) \Omega,$$

$$u = |\mathbf{k}_\perp| \lambda_{\text{mfp}} \sqrt{Z_i}, \quad (10)$$

$$\Omega = \begin{cases} 1 & \text{if } |\mathbf{k}_\perp \cdot \mathbf{v}_d|/\nu_{ei} < 1, \\ 0 & \text{elsewhere,} \end{cases}$$

where λ_{mfp} is the electron mean free path and where $A_{|\mathbf{k}|} = 1/2$ in the collisionless limit. As mentioned in Ref. 61, this correction can be used provided the acoustic wave frequency $|\omega_s| = |kv_d|$ remains smaller than the electron–ion collisional frequency ν_{ei} (momentum exchange). This condition is contained in the factor Ω, which

ensures that A_k recovers its collisionless value when the condition is not fulfilled. Although easily introduced in our theoretical estimates, this factor remains far more challenging to implement in a self-consistent numerical modeling where other laser–plasma effects are accounted for, in which case Ω is set to unity (see Sec. II B). Likewise, the Landau damping factor γ_0 in Eqs. (7) and (12) may be expressed in the collisionless limit (Landau) [Eq. (10) in Ref. 52] as in Sec. III. When collisional effects are not negligible, the fit introduced in Ref. 62 will be used, leading to a dependence of γ_0 on $|\mathbf{k}|$, as in Sec. IV B.

In the laboratory frame, the solution of Eq. (4) for $\gamma_0 < 1$, with the initial conditions $\delta n_e(t=0) = \partial_t \delta n_e(t=0) = 0$, reads

$$\frac{\delta n_e(\mathbf{k},t)}{n_e} = \alpha_k A_{|\mathbf{k}|} \frac{I_0 g(\mathbf{k})}{n_c v_g T_e} f(\mathbf{k},t), \qquad (11)$$

$$f(\mathbf{k},t) = 1 + a_+ e^{g_+ c_s |\mathbf{k}| t} - a_- e^{g_- c_s |\mathbf{k}| t}, \qquad (12)$$

$$a_\pm = \frac{-iM_0 \cos(\theta) - \gamma_0 \mp i\sqrt{1-\gamma_0^2}}{2i\sqrt{1-\gamma_0^2}}, \qquad (13)$$

$$g_\pm = -\gamma_0 \pm i\sqrt{1-\gamma_0^2} - iM_0 \cos(\theta). \qquad (14)$$

Here, $M_0 = |\mathbf{M}_0|$, where $\mathbf{M}_0$ and $\mathbf{v}_d$ are assumed to be normal to the main laser x axis. The combination of the above density fluctuations, written in Fourier space, with Eq. (1) implies an inverse Fourier transform and leads to

$$\frac{d\theta}{dx} = \frac{1}{k_0} \frac{d\langle \mathbf{k}_\perp \rangle_\perp}{dx} \cdot \frac{\mathbf{v}_d}{|\mathbf{v}_d|}$$
$$= \frac{-1}{2} \frac{n_e}{n_c} \frac{I_0}{n_c v_g T_e} \int \frac{d^2 \mathbf{k}}{(2\pi)^2} \frac{i\mathbf{k}\cdot\mathbf{v}_d}{|\mathbf{v}_d|} \alpha_k A_{|\mathbf{k}|} g(\mathbf{k}) f(\mathbf{k},t) \langle e^{i\mathbf{k}\cdot\mathbf{r}_\perp} \rangle_\perp. \qquad (15)$$

Hence, the estimation of $\langle e^{i\mathbf{k}\cdot\mathbf{r}_\perp} \rangle_\perp$ with Eq. (2) leads to the final beam bending rate, and this depends on the Fourier transform of the transverse intensity profile, $g(\mathbf{k})$. References 48 and 50 assume Gaussian beams, while Ref. 63 addresses RPP beams, in the asymptotic regime only. To avoid any assumption about the SSD beam

temporal spectrum, as in Refs. 64 and 65, we will simply relate the averaged SSD beam centroid deflection to the speckle contributions using Gaussian transient regime estimates.[52]

B. Gaussian speckle in three dimensions

Hence, using $g(\mathbf{k}) = \exp(-\mathbf{k}^2 \sigma^2/8)$ with $\sigma = \lambda_0 f_\sharp$ and assuming a y-aligned drift velocity, the deflection rate may be recast as

$$\frac{d\theta}{dx} = -\frac{n_e}{n_c} \frac{I_0}{2v_g n_c T_e} \frac{1}{\sigma} \mathcal{G}(t), \qquad (16)$$

with

$$\mathcal{G} = \frac{\sigma^3}{8\pi} \Im \int_{-\infty}^{\infty} dk\, k^2 A_k e^{-k^2\sigma^2/4}$$
$$\times \int_0^\pi d\theta\, \alpha_{k/f}[M_0 \cos(\theta)] \cos(\theta) f(k,t). \qquad (17)$$

Figure 1(a) illustrates the temporal evolution of a single 3D Gaussian speckle of f-number $f_\sharp = 8$ and wavelength $\lambda_0 = 0.35\ \mu m$ in a fully ionized carbon plasma as predicted by Eqs. (16) and (17). As expected,[52] the deflection is larger for a flow with $M_0 = 1$ (red lines) in the asymptotic limit $t > 100$ ps (where $d\theta/dx \simeq 0.2$ rad/mm, red solid line) than for $M_0 = 0.8$ or 1.2 (where $d\theta/dx \simeq 0.17$ rad/mm and ~0.02, blue and black solid lines, respectively). In the transient, however, the bending at resonance remains slightly weaker than for the case $M_0 = 0.8$ (black lines) or 1.2 (blue lines, $t < 10$ ps). As a corollary, the resonance of the hot spot bending rate around a Mach number of the order of unity is not noticeable during the transient.

C. Spatially and temporally smoothed laser beam

The propagation of a spatially and temporally smoothed laser beam in a flowing plasma, as shown in Ref. 44, exhibits a deflection of its centroid that can be related to the contribution of hot spots. Assuming that the speckles are independent and of Gaussian form, we may now relate the time-averaged beam centroid deflection rate to the contribution of the speckles (subscript s) through

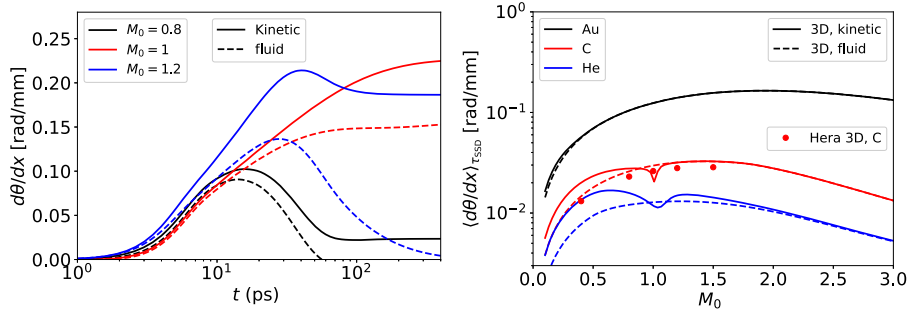$$\frac{d\theta_{SSD}}{dx} = \left\langle \sum_s \frac{d\theta_s}{dx} \right\rangle_t, \qquad (18)$$

FIG. 1. (a) Deflection rate $d\theta/dx$ as a function of time as predicted by Eqs. (16) and (17) for a C^{6+} plasma for various Mach numbers in the fluid [Eq. (7)] and kinetic formalism [Eq. (5)]. (b) Gaussian deflection rate averaged over $\tau_{SSD} = 7$ ps, $\langle d\theta/dx \rangle_{\tau_{SSD}}$, as predicted by Eqs. (19) and (23) (using $S = 1$ and $\beta = 1$) for He^{2+} (blue lines), C^{6+} (red lines), and Au^{50+} (black lines) plasmas as a function of Mach number. Three-dimensional predictions obtained with Hera are superimposed as red circles (see Appendix A for details). The laser has an averaged intensity of $I_0 = 1 \times 10^{15}$ W/cm², and $\lambda_0 = 0.35\ \mu m$, $f_\sharp = 8$, $T_e = 2.5$ keV, $T_i = 1$ keV, and $n_e = 0.1 n_c$.

where $\langle X \rangle_t$ is the average of X over a $2\pi/\omega_m$ period (where ω_m is the main modulation frequency of the SSD device). The speckle bending rate $d\theta_s/dx$ stems from Eq. (16). Owing to diffraction, σ and I_0 become $\sigma[1 + (x - x_s)^2/z_c^2]^{1/2}$ and $I_s/[1 + (x - x_s)^2/z_c^2]^{3/2}$, respectively. The speckle reaches its maximum intensity I_s at the position x_s and has a Rayleigh length of $z_c = \pi f_{\#}^2 \lambda_0$, leading to

$$\frac{d\theta_{\mathrm{SSD}}}{dx} = -S \frac{n_0}{n_c} \frac{I_0}{2v_g n_c T_e} \frac{\langle \mathcal{G} \rangle_{\tau_{\mathrm{SSD}}}}{\sigma}, \qquad (19)$$

where I_0 now denotes the beam-averaged intensity and where

$$S = \sum_s \frac{I_s/I_0}{[1 + (x - x_s)^2/z_c^2]^{3/2}}. \qquad (20)$$

The factor S introduced in Eqs. (19) and (20) incorporates the speckle-dependent factors such as the speckle intensities, spatial profiles, and positions. As S takes account of the complex RPP-induced speckle dynamics, we consider it as a parameter to be fitted from the paraxial simulations. This procedure further smooths out the hot spot contributions over the whole pulse. This approximation neglects the speckle disparities resulting from the variability of their intensity. Furthermore, we neglect any significant modification of the speckle distribution during the beam propagation, since this could affect the value of S. To mimic the effect of the SSD on the beam bending rate, the speckle pattern is assumed to last a time τ_{SSD}, proportional to the coherence time T_{SSD}. The latter is related to the modulation depth Δ (defined hereinafter at 3ω) and to the modulation frequency ω_m of the SSD device through $T_{\mathrm{SSD}} = 2\pi/\omega_m(2\Delta + 1)$. On introduction of the factor β, the parameter τ_{SSD}, referred to as the speckle coherence time, can be written as

$$\tau_{\mathrm{SSD}} = \beta \frac{2\pi}{\omega_m(2\Delta + 1)} = \beta T_{\mathrm{SSD}}. \qquad (21)$$

This second factor, of the order of unity, represents the efficiency of SSD in beam bending and will be deduced from the paraxial simulations.

We introduce the temporal mean of a function $X(t)$ over an SSD period as

$$\langle X \rangle_{\tau_{\mathrm{SSD}}} = \frac{1}{\tau_{\mathrm{SSD}}} \int_0^{\tau_{\mathrm{SSD}}} X(t)\,dt, \qquad (22)$$

Equation (17) leads to

$$\begin{aligned}
\langle \mathcal{G} \rangle_{\tau_{\mathrm{SSD}}} \simeq & \frac{\sigma^3}{8\pi} \Im \int_{-\infty}^{\infty} dk\, k^2 A_k e^{-k^2\sigma^2/4} \\
& \times \int_0^{\pi} d\theta\, \alpha_{k/f}[M_0 \cos(\theta)] \cos(\theta) \\
& \times \left(1 + a_+ \frac{e^{g_+ c_s |k| \tau_{\mathrm{SSD}}} - 1}{g_+ c_s |k| \tau_{\mathrm{SSD}}} - a_- \frac{e^{g_- c_s |k| \tau_{\mathrm{SSD}}} - 1}{g_- c_s |k| \tau_{\mathrm{SSD}}} \right).
\end{aligned} \qquad (23)$$

For the sake of simplicity, we propose in Appendix D a fully analytical fit of the above function, obtained in the fluid framework and valid in the regime $0.007 \leq \gamma_0 \leq 0.05$ and $|M_0| < 3$ for a monospecies plasma, illustrated in Figs. 7(a)–7(d).

The mean deflection angle is related to the set of Eqs. (18), (19), and (23). The dependences of the above predictions on the Mach number are illustrated in Fig. 1(b) for He^{2+} (blue lines),

C^{6+} (red lines), and Au^{50+} (black lines) 10% critical plasmas (with $T_e = 2.5$ keV and $T_i = 1$ keV) and for a speckle coherence time $\tau_{\mathrm{SSD}} = 7$ ps. The deflection rate is an increasing function of the ionization number, owing to the thermal correction of Eq. (10). By virtue of Sec. II B, the deflection rate is not peaked around $M_0 = 1$, owing to the short coherence time compared with the transient. A higher density causes the mean free path to decrease, thus increasing the local energy deposition and thereby enhancing the hole boring. The regime of validity of Eq. (10) ($\omega = kv_d < v_{ei}$), incorporated in the factor Ω, may be assessed by estimating the critical Mach number $M_c = v_{ei}/[c_s k_0/(2f_{\#})]$ above which the thermal correction is no longer valid. When $Z_i = 2$ (we obtain $M_c \sim 0.7$), the factor A_k is ~20% above its collisionless value, indicating a poor impact of thermal effects whatever the value of Ω. However, the carbon deflection rates exhibit slight inflections located around $M_0 = M_c \simeq 1.7$, due directly to the condition $\omega = kv_d < v_{ei}$. Additionally, the large value of $M_c \simeq 25$ obtained for the Au^{50+} case demonstrates the validity of the thermal corrections of Eq. (10) in this material.

Because of the very large values of $Z_i T_e/T_i$ in the gold case ($Z_i T_e/T_i = 125$), the kinetic and fluid 3D deflection rates (black and red lines respectively) are in agreement.[52] For the same reason, accounting for an accurate distribution of gold ionization levels under non-local-thermodynamic-equilibrium (NLTE) conditions as predicted by DEDALE[66] [in the multiple-ion-species formulation of Eq. (5)] leads to only a small reduction (by ~10%) of the final bending rates compared with the single-fluid average ionization number model as used in this study.

Finally, we performed five 3D hydrodynamic simulations with a paraxial solver (Hera[32,67]) of a Gaussian beam propagating in a C^{6+} 10%-critical plasma with the laser and plasma parameters of Fig. 1(b) and for various Mach numbers. The simulation parameters and the method of measuring the deflection rates are detailed in Appendix A. The thermal corrections of Eq. (10) (with Ω set to 1) have been accounted for. The average over the first 7 ps of the beam centroid deflection angles [$\langle\langle d\theta/dx \rangle_\perp \rangle_t$, Eqs. (2) and (22)] at the exit plane of the simulations are illustrated as red circles in Fig. 1(b) and agree very well with the corresponding theoretical prediction (obtained with $S = \beta = 1$) represented by the dashed red line. This confirms the validity of Eqs. (19) and (23) for a Gaussian beam. In the following, the time averaged centroid deflection rate of a SSD beam will be related to the above Gaussian speckle predictions by fitting the two scalar variables S and β using dedicated 3D paraxial numerical results.

III. FIT AND VALIDATION OF THE BENDING RATES BY PARAXIAL HYDRODYNAMIC SIMULATIONS

We aim at finalizing and validating our speckle-scale SSD beam bending model in light of paraxial 3D Parax[53] hydrodynamic simulations. We will thus use in this section the fluid plasma response in our model [Eq. (7)]. More realistic predictions, such as in Sec. IV B, will then be made using the kinetic deflection rates. Ideally, the kinetic flow-induced deflection should be fitted with kinetic codes (such as particle-in-cell codes)—a kind of simulation that is still out of reach with present supercomputers. In the Parax code, the linear Landau damping operator is computed in Fourier space,[50,68,69] and the light is propagated through a paraxial solver. Parax uses a linearized hydrodynamics module that is applied transversely to the main laser direction and that will moderate the subsequent required

numerical load. This approach is consistent with the fact that the density perturbation amplitudes considered in our model are always weak. For the sake of simplicity and for the purposes of comparison, the bremsstrahlung energy deposition is also neglected. Note that as the pulse deflection is reduced by its loss of temporal coherence, large simulation domains have to be considered in order to obtain clean quantitative comparisons. The thermal corrections of Eq. (10) are accounted for in our 3D simulations.

Parax has specific field injections and diagnostics to correctly simulate and characterize the different smoothing techniques. To reach more realistic ICF conditions than those in Ref. 52, the choice has been made to use a laser wavelength of $\lambda_0 = 0.35$ μm. The focal spot is located at the center of the simulation domain, $x_{\text{foc}} = 1$ mm, with a f-number $f_\sharp = 8.88$. The spectral dispersion has a modulation frequency $\omega_m = 2\pi \times 14.25$ GHz. The laser beam with $I_0 = 2 \times 10^{14}$ W/cm^2 propagates through a 2 mm flowing plasma with $v_d/c_s = 0.9$ and composed of helium with $n_e = 0.1n_c$, $T_e = 2$ keV, and $T_i = 500$ eV while accounting for the thermal corrections of Eq. (10). The simulation details are given in Appendix B. Different smoothing configurations have been simulated.

Owing to the phase modulation, the center of the beam oscillates as soon as it has been injected, with a period corresponding to the modulation frequency, $2\pi/\omega_m \simeq 70$ ps. This effect leads to periodic motion of the centroid at the simulation exit plane, as shown in Fig. 2. Note that the SSD beam bending model that we propose only predicts the temporal average of the beam centroid deflection, thus neglecting the motion of the spatial envelope.

The dependence of the beam's deflection angle on the f-number $f_\sharp$ is illustrated in Fig. 3(a). Note that we varied the f-number, keeping the mean intensity I_0 constant. Within the ansatz of Gaussian beam deflection, the latter should be proportional to $f_\sharp$ [see the integration of a Gaussian beam bending deflection rate over a Rayleigh length, Eq. (31) of Ref. 52]. However, under the assumption that S can be replaced by a constant, Eq. (19) predicts $\theta_{\text{SSD}} \propto \mathscr{G}(\tau_{\text{SSD}} c_s/f_\sharp \lambda_0)/f_\sharp = o(1/f_\sharp)$, as illustrated by the solid line in Fig. 3(a). Furthermore, although the speckle-scale contribution to the deflection increases with $f_\sharp$, the inter-speckle distance and the transient regime amplitude both depend on $f_\sharp$. Hence, smoothed over the whole SSD beam, the resulting centroid deviation decreases faster than $1/f_\sharp$ [see the dashed line in Fig. 3(a)]. Figure 3(a) also
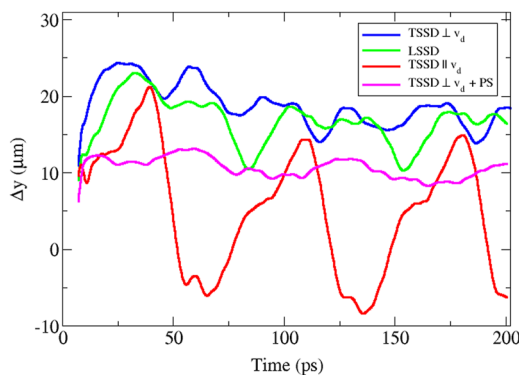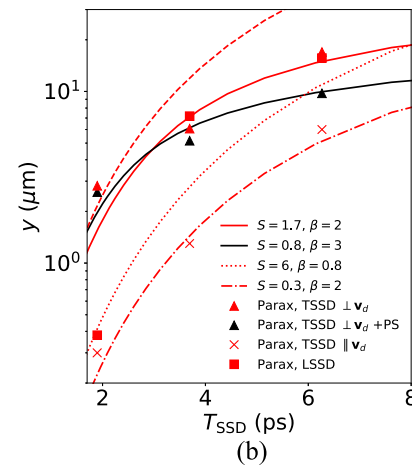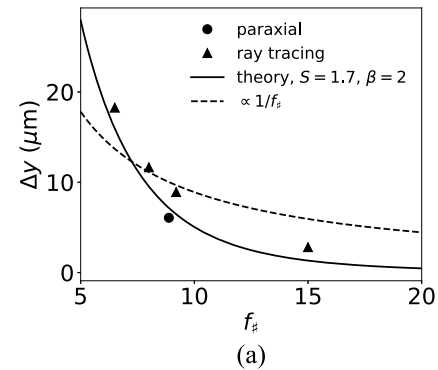
FIG. 3. Centroid displacement after 2 mm of propagation as predicted by the theory (lines) and by simulations (symbols). The plasma is composed of He^{2+} with $T_e = 2$ keV, $Z_i T_e/T_i = 8$, $M_0 = 0.9$, and $I_0 = 2 \times 10^{14}$ W/cm^2. In (a), the 2D centroid displacement Δy is plotted as a function of $f_\sharp$ with a fixed $T_{\text{SSD}} = 3.7$ ps (or a modulation depth of $\Delta = 9$), while in (b), $f_\sharp = 8.88$ is fixed and T_{SSD} varies. In (a), the predictions from the ray tracing scheme and from Eq. (19) with $S = 1.7$ and $\beta = 2$ are shown by the triangles and the black solid line, respectively. A curve of $y \propto 1/f_\sharp$ is superimposed as the black dashed line, while the results of the 3D paraxial Parax simulation for the case TSSD $\perp v_d$ are shown by the black circles. In (b), the predictions of Eq. (45) of Ref. 65 are shown by the red dashed line. The cases TSSD $\parallel v_d$, TSSD $\perp v_d$, and LSSD correspond to $(S, \beta) = (1.7, 1)$, $(1.7, 2)$, and $(S, \beta) = (6, 0.8)$, respectively. The case with PS corresponds to $(S, \beta) = (0.8, 3)$.

indicates that if the beam's effective f-number $f_\sharp$ were to decrease, as is to be expected when plasma smoothing occurs,[70] the resulting flow-induced deviation should be exacerbated.

We may now fit our model with the most relevant smoothing techniques in the light of the paraxial simulations performed with the Parax code.[53] In the case of 1D transverse smoothing by spectral dispersion (TSSD) oriented normally to the flow direction, our numerical results, represented by the red triangles in Fig. 3(b), confirm that the increase in SSD modulation depth (i.e., the decrease in T_{SSD}) reduces the amount of beam bending. Moreover, using $S = 1.7$ and $\beta = 2$ (solid lines) correctly reproduces the centroid deviations. Equation (45) of Ref. 65, represented by the red dashed line, predicts the deflection of a beam assuming a Gaussian frequency spectrum. Its spectral width is thus narrower than for a SSD laser beam. Consequently, the dependence of beam bending on the speckle coherence

FIG. 2. Temporal evolution of the beam centroid defined though Eq. (2) in the 3D Parax simulations with $\omega_m = 2\pi \times 14.25$ GHz and for $\Delta = 5.1$ for TSSD $\perp v_d$ (blue line), LSSD (green line), TSSD $\parallel v_d$ (red line), and TSSD $\perp v_d$ + PS (magenta line).

time is too steep and the predictions overestimate our numerical results for $\tau_{\text{SSD}} \gtrsim 5$ ps.

For the case in which the TSSD direction is parallel to the flow, Ref. 65 has found a significantly smaller deflection rate. The corresponding Parax simulations [crosses in Fig. 3(b)] exhibit a deflection rate roughly five times smaller than in the perpendicular configuration. In this case, the theoretical predictions with $S = 1.7$ and $\beta = 1$ give good agreement (dot-dashed line). Those two cases confirm that for a beam smoothed by 1D transverse SSD, such as on the NIF, different deviations are to be expected, depending on the direction of the flow relative to the smoothing direction. Indeed, when the direction of the spectral dispersion is perpendicular to the flow, the beam bending rate depends exclusively on the value of the flow. By contrast, when the direction of spectral dispersion is parallel to the flow, the speckles are moving along the flow with supersonic velocities. The relevant parameter to assess beam bending is the difference between the flow velocity and the transverse velocity of the speckles, Δv. In TSSD, the time evolution of the speckle transverse velocity is roughly sinusoidal.[71] For example, for $\Delta = 18$, the maximum transverse velocity reaches $v_y/c \sim 0.004$, which corresponds to $M \sim 3.3$. Δv then evolves rather quickly as a function of time, and is most of the time far from c_s, where the maximum of the deflection rate is located. This explains both the small time-averaged value of the beam bending and the important centroid oscillations with time that can be seen in Fig. 2, in which we represent the temporal evolution of the beam centroid for $\Delta = 5.1$ in the four simulated configurations for beam smoothing.

Additionally, the impact of PS has also been addressed for flows oriented normally to the transverse SSD direction. In our simulations, the polarizations in the near field are in the diagonal configuration, as for the inner cones on NIF.[72] Illustrated by black triangles in Fig. 3(b), our 3D Parax simulations agree fairly well with our model for $(S, \beta) = (0.8, 3)$. They also suggest a weak influence of the polarization smoothing on the bending rate when the coherence time is small ($T_{\text{SSD}} < 4$ ps). For longer coherence time ($\Delta = 5.1$), beam bending appears to be reduced when PS is used in the simulation. This reduction can be attributed either to the uncorrelated spatial speckle distribution between the two polarizations or to another nonlinear effect. Indeed, when PS is not used, beam spreading is noticeable in the simulation (the angular aperture is increased by ~20%, and the effective $f_\parallel$ decreases from 9 to 7.5). The increased beam bending in the absence of PS could be explained by the decrease in $f_\parallel$, as shown in Fig. 3(a). Given the weak influence of PS, the latter will be neglected when the flow is parallel to the transverse SSD direction.

The dependence of the bending rate on the angle between the flow component normal to the main laser axis and the SSD direction, ϕ, is outside the scope of this study. However, the value of β evolves from 1 to 2 when $\phi = 0$ (TSSD $\parallel \mathbf{v}_d$) and $\phi = \pi/2$ (TSSD $\perp \mathbf{v}_d$), respectively. The formula $\beta(\phi) = 1 + |\sin(\phi)|$ could be well suited to generalized the model to 3D.

Finally, another set of Parax simulations were performed with longitudinal temporal smoothing (LSSD), as used on the LMJ facility. In this configuration, the phase shift imposed between the different frequencies is radial, causing the speckles to move mainly longitudinally. The results are represented by the red squares in Fig. 3(b). The deflection rates are bounded by the two cases SSD $\perp \mathbf{v}_d$ and SSD $\parallel \mathbf{v}_d$, with the advantage of presenting a value independent

TABLE I. Values of the fitting parameters S and β to be used in Eq. (19).

	S	β
3D TSSD $\perp \mathbf{v}_d$	1.7	2
3D TSSD $\perp \mathbf{v}_d$ + PS	0.8	3
3D TSSD $\parallel \mathbf{v}_d$	1.7	1
3D TSSD $\parallel \mathbf{v}_d$ + PS	1.7	1
3D LSSD	6	0.8

of the flow direction. The use in our model of $(S, \beta) = (6, 0.8)$ leads to fair agreement.

LSSD is more efficient than TSSD for small coherence times only. The LMJ optimum modulation depth is close to 15 (defined for $\lambda_0 = 0.35$ μm) for $\omega_m = 2\pi \times 14.25$ GHz, leading to $\tau_{\text{SSD}} \simeq 2.26$ ps, and so for the parameters of Fig. 3(b), the overall LMJ deflection over 2 mm is ~1 μm. The NIF currently uses $\tau_{\text{SSD}} \simeq 6.5$ ps ($\omega_m = 2\pi \times 17$ GHz and $\Delta \sim 4$) with PS and thus corresponds to a larger deflection than that for the LMJ configuration (~10 and ~3 μm for flows perpendicular and parallel to the TSSD direction, respectively). As a result, the beam bending mitigation in high-energy laser experiments is efficiently done by increasing the laser's temporal spectral width. However, a large spectral width, apart from the associated FM–amplitude modulation (AM) conversion effect on laser performance,[73,74] may lead to anisotropic deflection rates when TSSD is used.

Before including the present theoretical calculations in a ray tracing scheme, we gather in Table I the values of the fitting parameters as obtained in the different geometries and SSD configurations.

IV. ACCOUNTING FOR BEAM BENDING WITH SPECTRAL DISPERSION IN RAY TRACING SCHEMES

A. Description and validation of the ray tracing scheme

The time-averaged centroid deviation rate may naturally be implemented in a ray tracing scheme as a correction to the well-known refraction effect arising from the eikonal equation, by deflecting each ray accordingly to Eq. (19). The ray direction and position $\mathbf{k}$ and $\mathbf{r}$, respectively therefore satisfy

$$\frac{d\mathbf{k}}{ds} = -k_0 \frac{\nabla n_e}{2n_c\eta} - k_0 S \frac{n_0}{n_c} \frac{I_0}{2v_g n_c T_e} \frac{\langle \mathcal{G} \rangle_{\tau_{\text{SSD}}}}{\sigma} \frac{\mathbf{v}_\perp}{|\mathbf{v}_\perp|},$$

$$\frac{d\mathbf{r}}{ds} = \frac{\mathbf{k} v_g}{\omega_0}, \tag{24}$$

$$\mathbf{v}_\perp = \mathbf{v}_d - \frac{\mathbf{v}_d \cdot \mathbf{k}}{|\mathbf{k}|^2} \mathbf{k},$$

where s is the ray abscissa and η the optical index.

The above model has been implemented in a new ray tracing module of the hydrodynamic code Hera.[32,67] For solving the ray trajectory, we split the rectangular meshes of the 2D Hera hydrodynamic module into four triangles using their diagonals. In each triangle, the density profile is assumed to be linear, allowing us to have a continuous density profile throughout the simulation

domain. Hence, solving the eikonal equation in each triangle allows us to split the ray trajectory into a sequence of parabolas, ideal for fast computing. Summing the contribution of each ray that passes through a given mesh following Ref. 43, we obtain the local averaged intensity I_0 used in Eq. (24). To circumvent the nonlinearity, we propose to use the local intensity calculated at the previous hydrodynamic time-step.

To mimic the averaged intensity profile at and off best focus, we define a lens position, hereinafter at $x_{lens} = -10$ m from which rays are shot. The rays' departure y positions on the lens are chosen randomly, and their initial direction points toward a randomly distributed position at the focal plane (at $x = x_{foc}$), following the measure given by the chosen intensity profile at best focus. Finally, the rays are propagated in vacuum from the lens to the left boundary condition of the simulation (at $x = x_{BC}$). To avoid statistical bias, the positions and directions of the rays are shot at the beginning of each time steps. Note that this procedure, as used in Ref. 38, prevents nonphysical thermal filamentation arising from systematic statistical errors induced by the fluctuations in laser ray number per cell.

Up to now, we have assumed $\mathbf{v}_d$ to be perpendicular to the main laser axis. For any flows, the axis along which the beam bending contribution in Eq. (24) lies results from the projection $\mathbf{v}_\perp$ of the fluid velocity $\mathbf{v}_d$ on the plane perpendicular to the beam main direction. Importantly, this modification to the classical ray tracing scheme [Eq. (24)] remains minimal, since it does not modify the main algorithm for ray propagation (described above), apart from adding a dependence on the beam intensity of the rays' trajectories. Equation (24) may be applied in a 2D ray tracing simulation performed in the $(\mathbf{k}_0, \mathbf{v}_d)$ plane (where $\mathbf{k}_0$ is the main laser axis) with the 3D beam bending deflection rates [and thus using $\langle \mathcal{G} \rangle_{\tau_{SSD}}$, Eq. (23), instead of its 2D equivalent]. Referred to subsequently as a 2.5D geometry, this will allow us to estimate the bending rate in a realistic geometry in a cheap 2D simulation.

To validate the implementation of the beam bending model in the ray tracing module of Hera, we performed four 2.5D ray tracing Hera simulations. A mesh size of $dx = 7.8$ μm and $dy = 4$ μm was used, along with 10^3 rays with various values of $f_\parallel$. All other simulation characteristics (equations of state, boundary conditions, and simulation domain) were identical to those of the paraxial simulations, as described in Sec. III. Illustrated as black triangles in Fig. 3(a), the centroid deviations resulting from the modified ray tracing module of Hera [using the fluid beam bending rate, Eqs. (7), (10), (19), and (23)] reproduce correctly the temporally averaged theoretical (solid lines) and paraxial (circles) predictions.

It is worth noting that restricting the model to the beam centroid deviation implies to neglect the contributions to beam spreading coming from the different deflections caused by the various speckle intensities and lifetimes. Likewise, the forward Brillouin instability[45,46,75] and associated plasma smoothing effects may contribute to reducing the effective speckle waist, thereby affecting the final beam centroid deviation.[70] Figure 3(a) demonstrates that the bending rate decreases faster than $1/f_\parallel$, and so plasma smoothing effects may greatly worsen the impact of beam bending on the propagation of the laser. Moreover, our crude modeling of the speckle dynamics does not account for the oscillations of the coherence time and speckle velocity as characterized in Ref. 76, which also contribute to the fluctuations in the beam direction.

B. Quantifying the beam bending of a realistic pulse in ICF conditions

To quantify the beam bending level under realistic conditions, we performed a 2D-axisymmetric hydrodynamic simulation with the Troll code (see Appendix C for details)[38] of Hybrid B NIF Shot N181209,[55–57] i.e., with a diamond ablator and a low-gas-fill hohlraum. No significant amounts of backscattering were measured during these shots, and so the beam bending may be addressed here independently from the stimulated backward Brillouin/Raman instability. One representative time was retained, 6 ns, which corresponds to the main power drive, as illustrated in Fig. 4(a). We will focus here on the beam bending of the inner cone, whose main axis
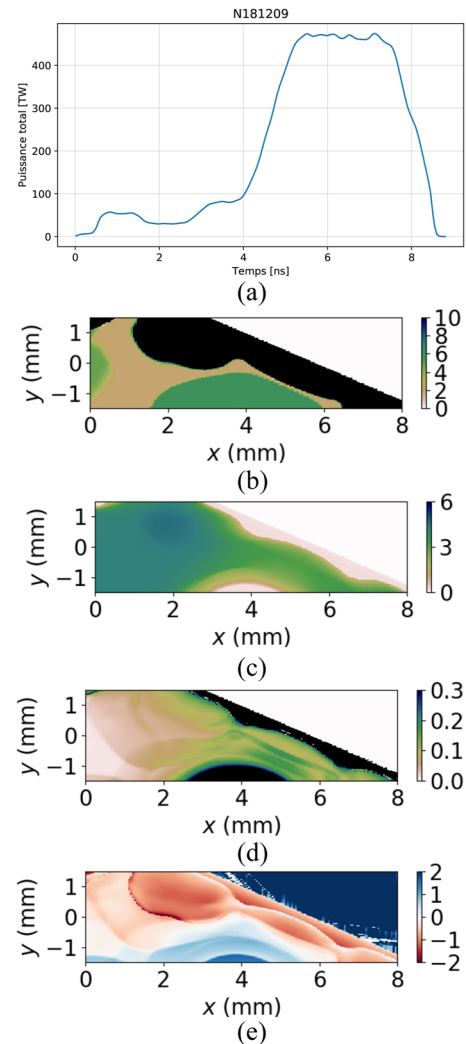
FIG. 4. Hydrodynamic simulation performed with the Troll code[38] for the Hybrid B NIF Shot N181209,[55–57] illustrated in the frame of the inner cone ($y = 0$ is the main inner cone axis), at 6 ns. (a) Total power of main laser drive. (b) Averaged local ionization number $\langle Z_i \rangle$ (the color map is saturated to 10). (c) Electron temperature T_e (keV). (d) Normalized electron density n_e/n_c (the color map is saturated to $n_e/n_c = 0.3$). (e) Mach number of the y component of the flow velocity, $\mathbf{v}_\perp/c_s$.

lies on $y = 0$ and propagates from left to right in Figs. 4(b)–4(e). The beam bending deflection rate is calculated using the local plasma and laser parameters ($f_\sharp = 8$), with a speckle coherence time $\tau_{SSD} = 7$ ps. Use is made of the 3D theoretical kinetic predictions of Eqs. (5), (19), and (23), together with the nonlocal correction of Eq. (10). Note that we do not use the analytical fit of $\langle \mathscr{G} \rangle_{\tau_{SSD}}$ presented in Appendix D, but we solve numerically the quadrature of Eq. (23). The TSSD direction is vertical in the NIF chamber,[72] and therefore its direction lies in the (r, z) plane of the hydrodynamic simulation. Owing to the weak effect of the PS, we will thus apply our deflection model with $(S, \beta) = (1.7, 1)$, according to Table I.

Figures 4(b)–4(e) show the local $\langle Z_i \rangle$, T_e, n_e/n_c, and y component of the flow velocity, respectively. Note that the color map in (b) is saturated to $\langle Z_i \rangle = 10$, and thus the high-Z gold medium is represented by the black areas. The map of the y component of velocity, normalized to the local acoustic speed, suggests that at 6 ns, helium, carbon, and gold, with electron densities ranging from $n_e \sim 0.05$ to $n_e \sim 0.2$, may be found on the inner beam path with $M_0 \sim 1$. Indeed, as the helium gas is being compressed by the expanding ablator [the green region in Fig. 4(b)] and gold wall [the black region in Fig. 4(b)], the electron density remains in the 10% critical density range. Likewise, the electron temperature, higher than 3 keV in these regions, leads to qualitatively small Landau damping rates and therefore to a bending not so far from its large asymptotic limit. Note that at 6 ns, the density of the expanded window is of the order of $n_e \sim 10^{-3} n_c$ [see Fig. 4(b)], which is too small for speckle-scale beam bending to occur.

We performed two 2.5D ray tracing Hera simulations using the plasma profiles from the Troll simulation at 6 ns. These simulations did not solve the hydrodynamic equations. We used a domain size of $L_x \times L_y = 8 \times 3$ mm^2, a mesh size of $dx = 9.7$ μm and $dy = 11.7$ μm, an f-number of $f_\sharp = 8$, and a beam waist of 1 mm. The beam was composed of 10^3 rays, and all the other simulation characteristics were identical to those of the paraxial simulations. Figures 5(a) and 5(c) present the intensity map and the inverse bremsstrahlung power of the inner cone with the modified scheme of Eq. (24). These are to be compared with the corresponding classical ray propagation results in Figs. 5(b) and 5(d). The intensity profiles evidence a weak impact of the beam bending dynamics on the pointing direction. When account is taken of the beam deviation [Fig. 5(a)], the expanding gold bubble around $x = 2$ mm tends to deflect the laser toward the ablator. Indeed, Fig. 5(e) shows the local 2.5D bending rate and reveals a slight deflection of ~ -70 mrad/mm located in the gold material. Likewise, the compressed helium and a small part of the ablator tend to deviate the other half of the beam (by $\sim +50$ mrad/mm) in the direction of the gold wall (upward), thus enhancing the already present focusing effect due to refraction. The temporal incoherence of the laser is thus not strong enough to totally suppress the beam bending and compensate for the thermal effects, especially in the gold medium, leading to significant deflection rates, as illustrated in Fig. 5(e). Quantitatively, the energy deposition is 0.5% weaker in the gold medium as extracted from our ray tracing simulation with our beam bending model than without it, and 10% less power is deposited onto the carbon ablator when the deviation is taken into account. However, the profile of the laser absorption is modified, being much more peaked around $(x, y) \simeq (4.5, 0)$ mm when the beam bending is included. Quantitatively, $\sim 0.05\%$ of the incoming laser power is able to leave the gold bubble in the presence of beam bending, which greatly contrasts with the $\sim 2.8 \times 10^{-4}\%$ obtained without flow-induced refraction. These
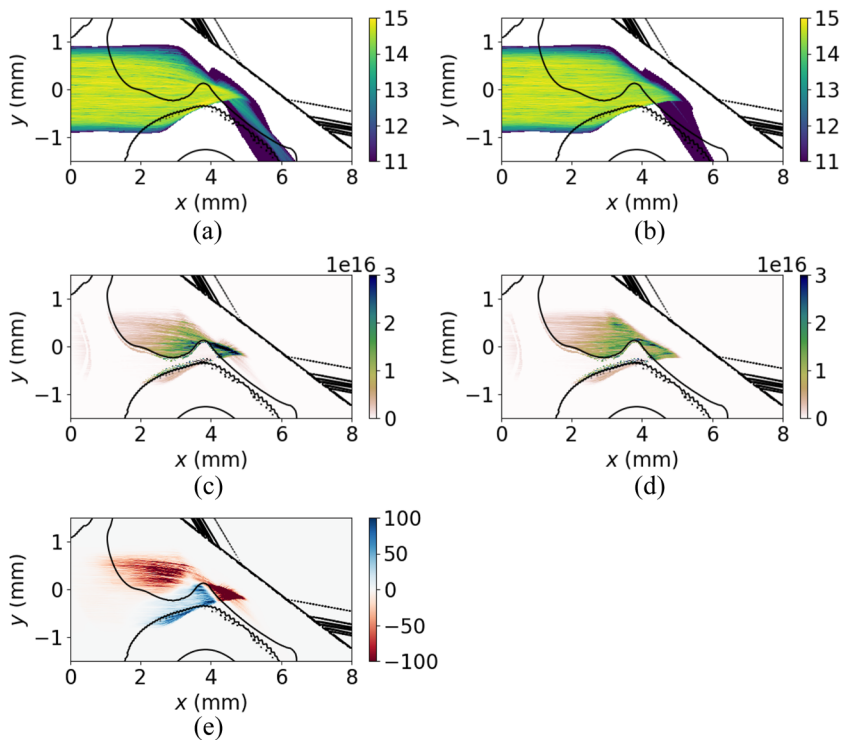

FIG. 5. (a) and (b) Intensity profiles $\log(I[\text{W/cm}^2])$. (c) and (d) Power deposited in the plasma through inverse bremsstrahlung, S_B (W/cm^2). (e) 2.5D deflection rate $d\theta_{SSD}/dx$ (mrad/mm) as predicted by Hera. (a), (c), and (e) show the results predicted by the 2.5D beam bending rate [Eq. (24) with $(S, \beta) = (1.7, 1)$], while (b) and (d) show the results from the classical ray tracing scheme. The material boundaries are superimposed as black lines.

numbers, highly sensitive to the beam bending model, seem to be at least qualitatively consistent with the measurements presented in another experiment.[77]

Importantly, the part of the beam that is specularly refracted by the gold wall is more energetic according to our model than when the classical ray tracing scheme is used [see Figs. 5(a) and 5(b) around $(x, y) \simeq (6, -1)$ mm]. The small flow-induced deflections in the gold bubble seem to be sufficient, at grating incidence, to significantly modify the penetration depth of the laser in the dense plasma and its absorption. The resulting deflected beam, of intensity in excess of 10^{13} W/cm^2, could reach the opposite laser entrance hall and therefore could lead to possible wave mixing with opposite-side beams. The striking qualitative similarity with experimental measurements ascribed to stimulated Brillouin side scatter or the so-called glint[77–79] indicates an urgent need to address the impact of beam bending on the implosion dynamics in ICF experiments.

V. CONCLUSIONS AND PROSPECTS

On the basis of previous work, we have addressed the beam bending physics of a realistic (RPP, SSD, and PS) high-energy laser beam propagating under ICF plasma conditions. By mean of large homogeneous paraxial hydrodynamic simulations, we have constructed a 3D ray-tracing model that quantitatively captures the temporally averaged centroid deviation of realistic beams. The use of our ray tracing model under ICF Hybrid B conditions reveals a weak modification of the beam propagation properties as a consequence of speckle-scale beam bending. Our results indicate that flow-induced deviation in the gold bubble is a good candidate for explaining the anomalous refraction measurements: the so-called glint.[78,79] Our model may thus be used to predict and assess the impact of this anomalous refraction on implosion dynamics and wave mixing processes. The impact of beam bending in other ICF scenarios is left for future work.

Speckle-scale physics may thus be included in a coarse description of laser light, such as ray tracing-based schemes, opening the way for a more realistic laser energy deposition model in radiative hydrodynamic codes. Obtaining more accurate predictions of the implosion symmetry and bang time without resorting to nonphysical artifacts such as laser power multipliers[80] may allow smart ICF designs[81,82] and possible control of deleterious laser–plasma effects.

Our ray tracing model with spectral dispersion has been compared with homogeneous ideal simulations, and so its validity can be ensured only in smooth density gradients. Furthermore, most wave-mixing processes are absent from our analysis, although these might possibly affect the beam deflection and thus bring further complexity to the system.[25] According to Fig. 3(a), the speckle-scale beam bending may be greatly amplified by plasma smoothing effects.[70,83] The ICF estimates in Figs. 5(a), 5(c), and 5(e) could thus represents a lower bound on the realistic flow-induced deflection. Since our study is limited to the beam centroid deviation, further analyses, including forward scattering and beam spreading,[46,48,84] are required to obtain a deeper understanding of all the physical mechanisms that can affect the beam pointing and subsequent laser energy deposition region inside the hohlraum.

Furthermore, our theory and simulations in realistic geometries allow a comparison of the efficiency of various temporal smoothing techniques that can be applied to achieve control of the beam pointing direction. Compared with LSSD, we have confirmed that 1D TSSD results in an anisotropic deflection rate. The latter can be substantially reduced by increasing the SSD modulation depth to reach field coherence times below 2 ps. Although outside the scope of this study, alternative smoothing strategies such as multicolored beams[85–87] could also be of interest with regard to the beam bending dynamics.

Finally, a ray tracing-based simulation incorporating our beam bending model would require evaluation of the quadrature of Eq. (23) each time a ray exits a cell. The exact calculations seem numerically too demanding unless one resorts to a tabulation of the deflection rates or to an accurate fit that would significantly alleviate the computational load. For that purpose, a fit is presented in Appendix D that should facilitate implementation of a ray tracing beam bending model in hydrodynamic codes. A radiative hydrodynamics simulation of a whole-capsule implosion using our beam bending model is left for future work.

AUTHOR DECLARATIONS

Conflict of Interest

The authors have no conflicts to disclose.

Author Contributions

C. Ruyer: Conceptualization (lead); Investigation (lead); Methodology (lead); Software (equal); Validation (equal); Writing – original draft (lead); Writing – review & editing (equal). **P. Loiseau**: Conceptualization (supporting); Methodology (supporting); Software (equal); Writing – review & editing (equal). **G. Riazuelo**: Software (equal); Validation (equal); Writing – original draft (supporting); Writing – review & editing (equal). **R. Riquier**: Software (equal); Writing – original draft (supporting); Writing – review & editing (supporting). **A. Debayle**: Conceptualization (supporting); Methodology (supporting); Writing – review & editing (equal). **P. E. Masson-Laborde**: Conceptualization (supporting); Methodology (supporting); Writing – review & editing (supporting). **O. Morice**: Writing – review & editing (supporting).

DATA AVAILABILITY

The data that support the findings of this study are available from the corresponding author upon reasonable request.

APPENDIX A: THREE-DIMENSIONAL HERA SIMULATION OF GAUSSIAN BEAM BENDING

To validate the predictions of Sec. II C, five 3D Hera simulations of Gaussian beams have been performed with a wavelength of $\lambda_0 = 0.35$ μm, a maximum intensity of $I_0 = 10^{15}$ W/cm^2 and an f-number $f_\parallel = 8$. The homogeneous fully ionized carbon plasma at 10% of the critical density has a drift velocity along the y direction at a Mach number $M_0 = 0.4$, 0.8, 1, 1.2, or 1.5, with (T_e, T_i) = (2.5, 1) keV. The size of the simulation domain is $L_x \times L_y \times L_z$ = 100 μm $\times$ (40 μm)^2 and is composed of 50×512^2 meshes. The laser is injected from the left boundary at $x = 0$, and its focal spot is located at $(x_{foc}, y_{foc}, z_{foc}) = (50$ μm, 0, 0). The laser has a constant temporal profile preceded by a 1 ps-long linear rise. Additionally, the Landau damping operator is calculated in the Fourier space transverse to the main laser direction,[50,68,69] and the thermal correction of Eq. (10) (while setting $\Omega = 1$) is accounted for.

The resulting intensity profiles at $t = 10$ ps, illustrated in Fig. 6, reveal a deviation of the beam toward the flow (y) direction. The theoretical predictions of Sec. II C, which we aim at validating here, gather all the x dependence of the bending rate into the fitting factor S. Hence, a comparison of the 3D Hera predictions with Eq. (19) requires that we remove from the simulation results the influence of the x-Gaussian laser profile. We thus start by isolating the x-dependent factors (waist and intensity), leading in 3D to

$$\frac{d\theta}{dx} \simeq \frac{d^2 y}{dx^2} = \frac{1}{[1 + (x - x_{foc})^2/z_c^2]^{3/2}} \frac{d\theta_0}{dx}, \quad (A1)$$

where $z_c = \pi f_\parallel^2 \lambda_0$, and $d\theta_0/dx$ is the part of the beam bending rate that is independent of x, thus corresponding to Eq. (16). Hence, for $d\theta/dx(x = 0) = y(x = 0) = 0$, the deviation is related to $d\theta_0/dx$ through

$$y \simeq \frac{1}{[1 + (L_x - x_{foc})^2/z_c^2]^{1/2}} \frac{L_x^2}{2} \frac{d\theta_0}{dx}. \quad (A2)$$

The value $S = 1$, imposed in Sec. II C, corresponds to a deviation that reads $y_0 = 0.5 L_x^2 d\theta_0/dx$. In summary, to extract the relevant time-averaged centroid deviation from our 3D Hera simulation, we first compute the centroid deviation $\langle y \rangle_\perp$ at the exit plane [using Eq. (2)], divide it by the factor $[1 + (L_x - x_{foc})^2/z_c^2]^{-1/2} \simeq 0.81$, and average the results between t_0 and $t_0 + 7$ ps. We use $t_0 = 1.3$ ps here to

account for the time required for the laser to reach the exit plane of the simulation (~0.3 ps) and the 1 ps linear rise of the laser time envelope.

APPENDIX B: THREE-DIMENSIONAL PARAX SIMULATIONS

The Parax code simulates the propagation of electromagnetic waves in a plasma.[88] The propagation of one fixed polarization electromagnetic wave is modeled by a single generalized scalar paraxial equation (B1) for the electric field amplitude E and a wave equation (B2) for the plasma response in the perpendicular (y, z) plane:

$$\left(2i \frac{\omega_0}{c^2} \partial_t + 2i k_0 \eta \partial_x + i \partial_x k_0 \eta + \nabla_\perp^2 - \frac{\omega_0^2}{c^2} \frac{n_e - n_{e0}}{n_c} - \frac{\nu_{ei} \omega_0 n_{e0}}{c^2 n_c} \right) E = 0. \quad (B1)$$

Here, ν_{ei} is the electron–ion collision frequency. Stimulated Raman and Brillouin backscattering do not occur, owing to the presence of a single paraxial incident wave. However, both filamentation and forward stimulated Brillouin scattering (FSBS) can grow and interact. The plasma density is modeled using a fluid description, where expansion to second order in the field perturbation leads to an ion-acoustic wave driven by ponderomotive and thermal effects:[88,89]

$$\left[(\partial_t + \nu + \nu_y \partial_y)^2 - c_s^2 \nabla_\perp^2 \right] \log\left(\frac{n_e}{n_{e0}} \right) = \frac{Z_i}{c m_i n_c} \nabla_\perp^2 (A_t I). \quad (B2)$$

Here, ν_y represents a transverse plasma drift assumed to be along the y axis, and ν is the ion-acoustic wave damping rate. The logarithm saturates the density response and thus impedes the blowup of the self-focusing process that would otherwise be induced by the cubically nonlinear Schrödinger equation derived from Eq. (B1). Equation (B2) uses the acoustic type of plasma response and accounts for the plasma heating using a nonlocal electron transport model according to Ref. 59. The operator A_t in the source term is applied to the laser intensity; it accounts for the inverse bremsstrahlung heating, the ponderomotive effect, and the nonlocal transport. Its spectrum in Fourier space for the transverse spatial coordinates (y, z) uses the fit introduced in Ref. 59.

In the case of PS smoothing, the code models the propagation of two independent electromagnetic waves (the first polarized along the y axis and the second along the z axis), but the source term in Eq. (B2) is computed with the contributions of both electromagnetic waves.

Equation (B2) has been derived using the small-amplitude density and temperature hypothesis, namely, $dn_e/n_e \ll 1$ and $dT_e/T_e \ll 1$, and the quasistationary temperature hypothesis, namely, $dt(T_e) < \nu_{ei} I_0/c n_c$. In our simulations, the laser propagates into a 2 mm helium plasma that is assumed to be uniform with density $n_e(t = 0) = 0.1 n_c$, $T_e = 2$ keV, and $T_i = 0.5$ keV. The Landau damping rate has been determined by a kinetic dispersion solver, and its value is $\gamma_0 = 0.031$. The laser's average intensity is $\langle I_0 \rangle = 2 \times 10^{14}$ W/cm^2. This relatively small value has been chosen to limit the angular spread of the beam. The transverse and longitudinal mesh sizes are $dy = dz = 0.75 \lambda_0$ (for $\lambda_0.35$ μm) and $dx = 1.6$ μm, respectively.
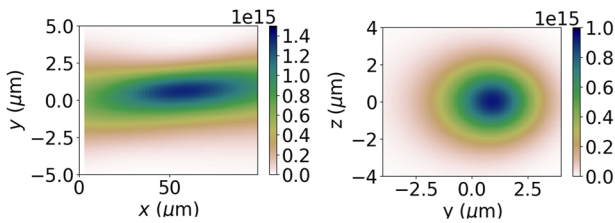
FIG. 6. Intensity profiles (W/cm^2) of a 3D Gaussian laser pulse propagating through a flowing ($M_0 = 0.8$) fully ionized carbon plasma at 10% to the critical density as predicted by 3D Hera simulations. (a) Intensity profile in the (x, y) plane, with the flow velocity along the y axis and the main laser direction along the x axis. (b) Intensity profile in the exit plane.

APPENDIX C: AXISYMMETRIC 2D SIMULATION WITH TROLL

Troll is a 3D arbitrary Lagrangian–Eulerian (ALE) radiative hydrodynamic code with unstructured mesh.[38] The simulation presented in Sec. IV B was performed in an axisymmetric 2D geometry. We used the latest CEA tabulated equations for state and opacities, with a model for NLTE correction of the emissivity. The radiation transport was solved using an implicit Monte Carlo method and the heat flux using the Spitzer–Härm model, limited to 10% of the freestreaming flux. The lasers were simulated using the classical 3D ray tracing method (without the beam bending model), with inverse bremsstrahlung absorption, corrected to account for the Langdon effect. Both Raman and Brillouin backscattering were measured to be just a few percent, and therefore were not taken into account. No multipliers were used on the incident laser power.

TABLE II. Polynomial coefficients $a_{n,m}$, $b_{n,m}$, $c_{n,m}$ in Eqs. (D2)–(D4).

$a_{n,m}$	$m = 0$	$m = 1$	$m = 2$	$m = 3$	$m = 4$
$n = 0$	0.025 488	−0.368 322	1.224 227	−0.549 216	0.050 112
$n = 1$	0.001 769	−0.043 288	0.403 904	−1.498 338	0.667 592
$n = 2$	−0.113 853	1.603 793	−5.426 916	6.871 689	−2.396 718
$n = 3$	0.189 056	−2.603 449	8.606 094	−10.111 674	3.370 095
$b_{n,m}$	$m = 0$	$m = 1$	$m = 2$	$m = 3$	$m = 4$
$n = 0$	−0.007 621	0.118 956	−0.355 869	0.163 322	0.015 022
$n = 1$	−0.088 640	1.126 735	−3.103 982	3.160 460	−1.086 508
$n = 2$	0.338 779	−4.382 979	12.275 832	−12.029 22	3.862 822
$n = 3$	−0.448 077	5.745 170	−16.150 09	15.789 91	−5.007 789
$c_{n,m}$	$m = 0$	$m = 1$	$m = 2$	$m = 3$	$m = 4$
$n = 0$	10.029 76	−22.232 38	26.037 80	−14.192 60	2.822 304
$n = 1$	9.268 230	−42.285 02	70.621 96	−45.765 98	10.012 57
$n = 2$	−373.594 7	1 539.699	−2 128.128	1 200.225	−237.254 0
$n = 3$	4444.712	−18 357.01	25 459.51	−14 404.95	2854.991

(a)

(b)

(c)

(d)
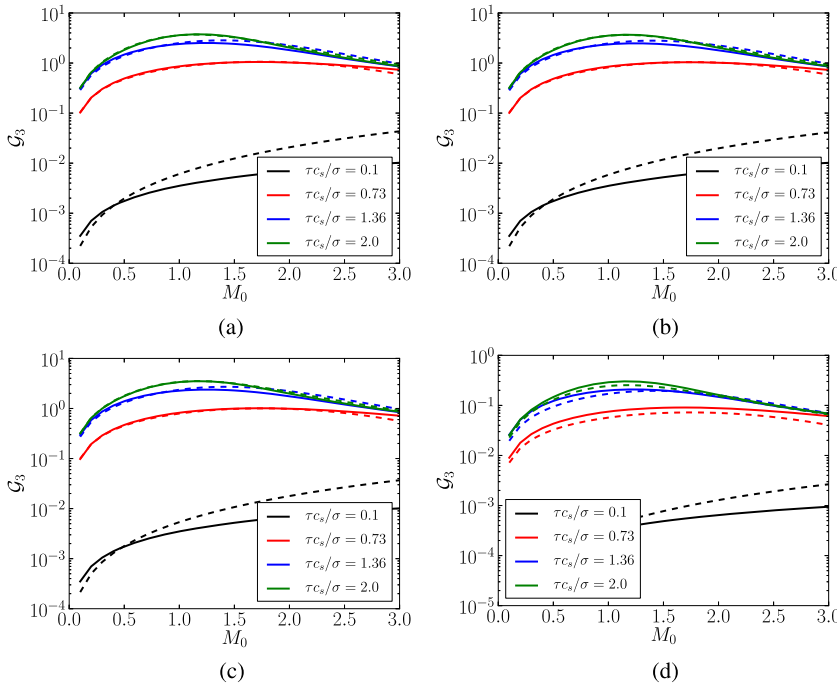
FIG. 7. Comparison between the fit of Eq. (D1) (dashed lines) and the exact calculations (solid lines) for different values of τ_{SSD}. The parameters in (a)–(c) correspond to a gold plasma ($Z_{Au} = 50$, $\lambda_{mfp}/f_{\#}\lambda_0 = 1.47$) with $\gamma_0 = 0.007$, 0.02, and 0.05, respectively, and those in (d) to a carbon plasma ($Z_C = 6$, $\lambda_{mfp}/f_{\#}\lambda_0 = 71$) with $\gamma_0 = 0.05$. $T_e = 3$ keV and $n_e = 9 \times 10^{26}$ m^{-3}.

APPENDIX D: FIT OF EQ. (23) IN THE FLUID FRAMEWORK

In order to facilitate the implementation of the present beam bending model in a hydrodynamic code, we introduce here a fit of the function $\langle \mathcal{G} \rangle_{\tau_{SSD}}$ [Eq. (23)] that appears in the ray tracing model of Eq. (24). We propose to use the following function defined in the domain $M_0 > 0$, with $k_c = 2^{1/2}/f_\sharp \lambda_0$,

$$\mathcal{G}_3 = \frac{A_{k_c}}{2} \frac{aM_0 + bM_0^2}{1 + (M_0/c)^4} \qquad (D1)$$

where a, b and c are polynomial functions of $\tau_{SSD}c_s/f_\sharp \lambda_0$ and γ_0. They follow,

$$a = \sum_{n=0}^{3} \sum_{m=0}^{4} a_{n,m} \gamma_0^n \left(\frac{\tau_{SSD}c_s}{f_\sharp \lambda_0} \right)^m, \qquad (D2)$$

$$b = \sum_{n=0}^{3} \sum_{m=0}^{4} b_{n,m} \gamma_0^n \left(\frac{\tau_{SSD}c_s}{f_\sharp \lambda_0} \right)^m, \qquad (D3)$$

$$c = \sum_{n=0}^{3} \sum_{m=0}^{4} c_{n,m} \gamma_0^n \left(\frac{\tau_{SSD}c_s}{f_\sharp \lambda_0} \right)^m. \qquad (D4)$$

The value of the coefficients $a_{n,m}$, $b_{n,m}$, $c_{n,m}$ are given in Table I. We retain the predictions of the above fit when $\mathcal{G}_3(M_0) > 0$ and set it to zero elsewhere. We also use $\mathcal{G}_3(-M_0) = -\mathcal{G}_3(M_0)$ in the negative Mach number domain. As shown in Fig. 7, this fit works fairly correctly in the domain $0.007 \leq \gamma_0 \leq 0.05$, $|M_0| < 2.53$ and $0.1 \leq \tau_{SSD}c_s/f_\sharp \lambda_0 \leq 2$ in a mono-species plasma, as shown in Figs. 7(a)–7(d).

REFERENCES

[1] R. P. Drake, "Introduction to high-energy-density physics," in *High-Energy-Density Physics: Fundamentals, Inertial Fusion, and Experimental Astrophysics*, edited by L. Davison and Y. Horie (Springer, Berlin, Heidelberg, 2006), pp. 1–17.

[2] J. D. Lindl, P. Amendt, R. L. Berger, S. G. Glendinning, S. H. Glenzer, S. W. Haan, R. L. Kauffman, O. L. Landen, and L. J. Suter, "The physics basis for ignition using indirect-drive targets on the National Ignition Facility," Phys. Plasmas **11**, 339–491 (2004).

[3] C. Cavailler, "Inertial fusion with the LMJ," Plasma Phys. Controlled Fusion **47**, B389–B403 (2005).

[4] K. Lan, Y. Dong, J. Wu, Z. Li, Y. Chen, H. Cao, L. Hao, S. Li, G. Ren, W. Jiang, C. Yin, C. Sun, Z. Chen, T. Huang, X. Xie, S. Li, W. Miao, X. Hu, Q. Tang, Z. Song, J. Chen, Y. Xiao, X. Che, B. Deng, Q. Wang, K. Deng, Z. Cao, X. Peng, X. Liu, X. He, J. Yan, Y. Pu, S. Tu, Y. Yuan, B. Yu, F. Wang, J. Yang, Y. Jiang, L. Gao, J. Xie, W. Zhang, Y. Liu, Z. Zhang, H. Zhang, Z. He, K. Du, L. Wang, X. Chen, W. Zhou, X. Huang, H. Guo, K. Zheng, Q. Zhu, W. Zheng, W. Y. Huo, X. Hang, K. Li, C. Zhai, H. Xie, L. Li, J. Liu, Y. Ding, and W. Zhang, "First inertial confinement fusion implosion experiment in octahedral spherical hohlraum," Phys. Rev. Lett. **127**, 245001 (2021).

[5] Y. R. Shen and N. Bloembergen, "Theory of stimulated Brillouin and Raman scattering," Phys. Rev. **137**, A1787 (1965).

[6] D. W. Forslund, J. M. Kindel, and E. L. Lindman, "Nonlinear behavior of stimulated Brillouin and Raman scattering in laser-irradiated plasmas," Phys. Rev. Lett. **30**, 739 (1973).

[7] Z. J. Liu, S.-p. Zhu, L. H. Cao, C. Y. Zheng, X. T. He, and Y. Wang, "Enhancement of backward Raman scattering by electron-ion collisions," Phys. Plasmas **16**, 112703 (2009).

[8] L. Hao, Z. J. Liu, X. Y. Hu, and C. Y. Zheng, "Competition between the stimulated Raman and Brillouin scattering under the strong damping condition," Laser Part. Beams **31**, 203–209 (2013).

[9] L. Hao, X. Y. Hu, C. Y. Zheng, B. Li, J. Xiang, and Z. J. Liu, "Study of crossed-beam energy transfer process with large crossing angle in three-dimension," Laser Part. Beams **34**, 270–275 (2016).

[10] D. F. DuBois, D. A. Russell, and H. A. Rose, "Saturation spectra of the two-plasmon decay instability," Phys. Rev. Lett. **74**, 3983 (1995).

[11] D. A. Russell and D. F. DuBois, "$\frac{3}{2}\omega_0$ radiation from the laser-driven two-plasmon decay instability in an inhomogeneous plasma," Phys. Rev. Lett. **86**, 428 (2001).

[12] D. F. DuBois, B. Bezzerides, and H. A. Rose, "Collective parametric instabilities of many overlapping laser beams with finite bandwidth," Phys. Fluids B **4**, 241–251 (1992).

[13] C. Z. Xiao, H. B. Zhuo, Y. Yin, Z. J. Liu, C. Y. Zheng, and X. T. He, "Linear theory of multibeam parametric instabilities in homogeneous plasmas," Phys. Plasmas **26**, 062109 (2019).

[14] J. Qiu, L. Hao, L. Cao, and S. Zou, "Collective stimulated Brillouin scattering modes of two crossing laser beams with shared scattered wave," Matter Radiat. Extremes **6**, 065903 (2021).

[15] W. G. Wagner, H. A. Haus, and J. H. Marburger, "Large-scale self-trapping of optical beams in the paraxial ray approximation," Phys. Rev. **175**, 256 (1968).

[16] Y. Kato, K. Mima, N. Miyanaga, S. Arinaga, Y. Kitagawa, M. Nakatsuka, and C. Yamanaka, "Random phasing of high-power lasers for uniform target acceleration and plasma instability suppression," Phys. Rev. Lett. **53**, 1057 (1984).

[17] S. Skupsky, R. W. Short, T. Kessler, R. S. Craxton, S. Letzring, and J. M. Soures, "Improved laser-beam uniformity using the angular dispersion of frequency-modulated light," J. Appl. Phys. **66**, 3456 (1989).

[18] N. D. Delamater, T. J. Murphy, A. A. Hauer, R. L. Kauffman, A. L. Richard, E. L. Lindman, G. R. Magelssen, B. H. Wilde, D. B. Harris, B. A. Failor, J. Wallace, L. V. Powers, S. M. Pollaine, L. J. Suter, R. Chrien, T. D. Shepard, H. A. Rose, E. A. Williams, M. B. Nelson, M. D. Cable, J. B. Moore, M. A. Salazar, and K. Gifford, "Symmetry experiments in gas-filled hohlraums at NOVA," Phys. Plasmas **3**, 2022–2028 (1996).

[19] G. Huser, C. Courtois, and M.-C. Monteil, "Wall and laser spot motion in cylindrical hohlraums," Phys. Plasmas **16**, 032703 (2009).

[20] R. Epstein and R. S. Craxton, "Statistical ray tracing in plasmas with random density fluctuations," Phys. Rev. A **33**, 1892–1902 (1986).

[21] J. D. Moody, B. J. MacGowan, D. E. Hinkel, W. L. Kruer, E. A. Williams, K. Estabrook, R. L. Berger, R. K. Kirkwood, D. S. Montgomery, and T. D. Shepard, "First optical observation of intensity dependent laser beam deflection in a flowing plasma," Phys. Rev. Lett. **77**, 1294–1297 (1996).

[22] A. Debayle, P.-E. Masson-Laborde, C. Ruyer, M. Casanova, and P. Loiseau, "Cross-beam energy transfer: On the accuracy of linear stationary models in the linear kinetic regime," Phys. Plasmas **25**, 052702 (2018).

[23] M. Duluc, D. Penninckx, P. Loiseau, G. Riazuelo, A. Bourgeade, A. Chatagnier, and E. D'humières, "Comparison of longitudinal and transverse smoothing by spectral dispersion on stimulated Brillouin backscattering in inertial confinement fusion plasmas," Phys. Plasmas **26**, 042707 (2019).

[24] L. Yin, B. J. Albright, D. J. Stark, W. D. Nystrom, R. F. Bird, and K. J. Bowers, "Saturation of cross-beam energy transfer for multispeckled laser beams involving both ion and electron dynamics," Phys. Plasmas **26**, 082708 (2019).

[25] S. Hüller, G. Raj, W. Rozmus, and D. Pesme, "Crossed beam energy transfer in the presence of laser speckle ponderomotive self-focusing and nonlinear sound waves," Phys. Plasmas **27**, 022703 (2020).

[26] S. Laffite and P. Loiseau, "Design of an ignition target for the laser megajoule, mitigating parametric instabilities," Phys. Plasmas **17**, 102704 (2010).

[27] P. E. Masson-Laborde, M. C. Monteil, V. Tassin, F. Philippe, P. Gauthier, A. Casner, S. Depierreux, C. Neuville, B. Villette, S. Laffite, P. Seytor, P. Fremerye, W. Seka, D. Teychenné, A. Debayle, D. Marion, P. Loiseau, and M. Casanova, "Laser plasma interaction on rugby hohlraum on the Omega Laser Facility: Comparisons between cylinder, rugby, and elliptical hohlraums," Phys. Plasmas **23**, 022703 (2016).

[28] K. Glize, C. Rousseaux, D. Bénisti, V. Dervieux, L. Gremillet, S. D. Baton, and L. Lancia, "Stimulated backward Raman scattering driven collectively by two

picosecond laser pulses in a bi- or multi-speckle configuration," Phys. Plasmas **24**, 032708 (2017).

[29]B. J. Winjum, A. Tableman, F. S. Tsung, and W. B. Mori, "Interactions of laser speckles due to kinetic stimulated Raman scattering," Phys. Plasmas **26**, 112701 (2019).

[30]R. L. Berger, B. F. Lasinski, A. B. Langdon, T. B. Kaiser, B. B. Afeyan, B. I. Cohen, C. H. Still, and E. A. Williams, "Influence of spatial and temporal laser beam smoothing on stimulated Brillouin scattering in filamentary laser light," Phys. Rev. Lett. **75**, 1078 (1995).

[31]C. H. Still, R. L. Berger, A. B. Langdon, D. E. Hinkel, L. J. Suter, and E. A. Williams, "Filamentation and forward Brillouin scatter of entire smoothed and aberrated laser beams," Phys. Plasmas **7**, 2023 (2000).

[32]P. Loiseau, O. Morice, D. Teychenné, M. Casanova, S. Hüller, and D. Pesme, "Laser-beam smoothing induced by stimulated Brillouin scattering in an inhomogeneous plasma," Phys. Rev. Lett. **97**, 205001 (2006).

[33]S. Hüller, P. E. Masson-Laborde, D. Pesme, M. Casanova, F. Detering, and A. Maximov, "Harmonic decomposition to describe the nonlinear evolution of stimulated Brillouin scattering," Phys. Plasmas **13**, 022703 (2006).

[34]S. Hüller, G. Raj, M. Luo, W. Rozmus, and D. Pesme, "Crossed beam energy transfer between optically smoothed laser beams in inhomogeneous plasmas," Philos. Trans. R. Soc., A **378**, 20200038 (2020).

[35]M. M. Marinak, G. D. Kerbel, N. A. Gentile, O. Jones, D. Munro, S. Pollaine, T. R. Dittrich, and S. W. Haan, "Three-dimensional HYDRA simulations of National Ignition Facility targets," Phys. Plasmas **8**, 2275–2280 (2001).

[36]Z. Qinghong, P. Wenbing, C. Juan, Y. Heng, and Z. Chuanlei, "Radiation hydrodynamics code LARED-H for laser fusion simulation," in *Competence in High Performance Computing 2010*, edited by C. Bischof, H.-G. Hegering, W. E. Nagel, and G. Wittum (Springer, Berlin, Heidelberg, 2012), pp. 227–234.

[37]H. Zhang, D. Yang, P. Song, S. Zou, Y. Zhao, S. Li, Z. Li, L. Guo, F. Wang, X. Peng, H. Wei, T. Xu, W. Zheng, P. Gu, W. Pei, S. Jiang, and Y. Ding, "X-ray conversion efficiency and radiation non-uniformity in the hohlraum experiments at Shenguang-III prototype laser facility," Phys. Plasmas **21**, 112709 (2014).

[38]E. Lefebvre, S. Bernard, C. Esnault, P. Gauthier, A. Grisollet, P. Hoch, L. Jacquet, G. Kluth, S. Laffite, S. Liberatore, I. Marmajou, P.-E. Masson-Laborde, O. Morice, and J.-L. Willien, "Development and validation of the TROLL radiation-hydrodynamics code for 3D hohlraum calculations," Nucl. Fusion **59**, 032010 (2018).

[39]R. A. Egorchenkov and Y. A. Kravtsov, "Complex ray-tracing algorithms with application to optical problems," J. Opt. Soc. Am. A **18**, 650 (2001).

[40]A. Colaïtis, G. Duchateau, P. Nicolaï, and V. Tikhonchuk, "Towards modeling of nonlinear laser-plasma interactions with hydrocodes: The thick-ray approach," Phys. Rev. E **89**, 033101 (2014).

[41]D. J. Strozzi, D. S. Bailey, P. Michel, L. Divol, S. M. Sepke, G. D. Kerbel, C. A. Thomas, J. E. Ralph, J. D. Moody, and M. B. Schneider, "Interplay of laser-plasma interactions and inertial fusion hydrodynamics," Phys. Rev. Lett. **118**, 025002 (2017).

[42]A. Colaïtis, J. P. Palastro, R. K. Follett, I. V. Igumenschev, and V. Goncharov, "Real and complex valued geometrical optics inverse ray-tracing for inline field calculations," Phys. Plasmas **26**, 032301 (2019).

[43]A. Debayle, C. Ruyer, O. Morice, P.-E. Masson-Laborde, P. Loiseau, and D. Benisti, "A unified modeling of wave mixing processes with the ray tracing method," Phys. Plasmas **26**, 092705 (2019).

[44]D. E. Hinkel, E. A. Williams, and C. H. Still, "Laser beam deflection induced by transverse plasma flow," Phys. Rev. Lett. **77**, 1298–1301 (1996).

[45]M. Grech, V. T. Tikhonchuk, G. Riazuelo, and S. Weber, "Plasma induced laser beam smoothing below the filamentation threshold," Phys. Plasmas **13**, 093104 (2006).

[46]M. Grech, G. Riazuelo, D. Pesme, S. Weber, and V. T. Tikhonchuk, "Coherent forward stimulated-Brillouin scattering of a spatially incoherent laser beam in a plasma and its effect on beam spray," Phys. Rev. Lett. **102**, 155001 (2009).

[47]C. Rousseaux, K. Glize, S. D. Baton, L. Lancia, D. Bénisti, and L. Gremillet, "Experimental evidence of backward Raman scattering driven cooperatively by two picosecond laser pulses propagating side by side," Phys. Rev. Lett. **117**, 015002 (2016).

[48]D. E. Hinkel, E. A. Williams, R. L. Berger, L. V. Powers, A. B. Langdon, and C. H. Still, "Propagation of realistic beams in underdense plasma," Phys. Plasmas **5**, 1887–1894 (1998).

[49]B. Bezzerides, "Intrinsic bending of a laser beam in a flowing plasma," Phys. Plasmas **5**, 2712–2720 (1998).

[50]H. A. Rose, "Laser beam deflection by flow and nonlinear self-focusing," Phys. Plasmas **3**, 1709–1727 (1996).

[51]D. S. Montgomery, R. P. Johnson, H. A. Rose, J. A. Cobble, and J. C. Fernández, "Flow-induced beam steering in a single laser hot spot," Phys. Rev. Lett. **84**, 678–681 (2000).

[52]C. Ruyer, A. Debayle, P. Loiseau, M. Casanova, and P. E. Masson-Laborde, "Kinetic analytical modeling of Gaussian pulse beam-bending including the transient regime," Phys. Plasmas **27**, 102105 (2020).

[53]G. Riazuelo and G. Bonnaud, "Coherence properties of a smoothed laser beam in a hot plasma," Phys. Plasmas **7**, 3841–3844 (2000).

[54]O. A. Hurricane, P. T. Springer, P. K. Patel, D. A. Callahan, K. Baker, D. T. Casey, L. Divol, T. Döppner, D. E. Hinkel, M. Hohenberger, L. F. Berzak Hopkins, C. Jarrott, A. Kritcher, S. Le Pape, S. Maclaren, L. Masse, A. Pak, J. Ralph, C. Thomas, P. Volegov, and A. Zylstra, "Approaching a burning plasma on the NIF," Phys. Plasmas **26**, 052704 (2019).

[55]A. L. Kritcher, D. T. Casey, C. A. Thomas, A. B. Zylstra, M. Hohenberger, K. Baker, S. Le Pape, B. Bachmann, S. Bhandarkar, J. Biener, T. Braun, D. Clark, L. Divol, T. Döppner, D. Hinkel, C. Kong, D. Mariscal, M. Millot, J. Milovich, A. Nikroo, A. Pak, N. Rice, H. Robey, M. Stadermann, J. Sevier, D. Strozzi, C. Weber, C. Wild, B. Woodworth, J. Edwards, D. A. Callahan, and O. A. Hurricane, "Symmetric fielding of the largest diamond capsule implosions on the NIF," Phys. Plasmas **27**, 052710 (2020).

[56]A. B. Zylstra, D. T. Casey, A. Kritcher, L. Pickworth, B. Bachmann, K. Baker, J. Biener, T. Braun, D. Clark, V. Geppert-Kleinrath, M. Hohenberger, C. Kong, S. Le Pape, A. Nikroo, N. Rice, M. Rubery, M. Stadermann, D. Strozzi, C. Thomas, P. Volegov, C. Weber, C. Wild, C. Wilde, D. A. Callahan, and O. A. Hurricane, "Hot-spot mix in large-scale HDC implosions at NIF," Phys. Plasmas **27**, 092709 (2020).

[57]M. Hohenberger, D. T. Casey, A. L. Kritcher, A. Pak, A. B. Zylstra, C. A. Thomas, K. L. Baker, S. Le Pape, B. Bachmann, R. L. Berger, J. Biener, D. S. Clark, L. Divol, T. Döppner, V. Geppert-Kleinrath, D. Hinkel, H. Huang, C. Kong, O. L. Landen, J. Milovich, A. Nikroo, N. Rice, H. Robey, M. Schoff, J. Sevier, K. Sequoia, M. Stadermann, D. Strozzi, P. L. Volegov, C. Weber, C. Wild, B. Woodworth, D. A. Callahan, and O. A. Hurricane, "Integrated performance of large HDC-capsule implosions on the National Ignition Facility," Phys. Plasmas **27**, 112704 (2020).

[58]B. D. Fried, M. Gell-Mann, J. D. Jackson, and H. W. Wyld., "Longitudinal plasma oscillation in an electric field," J. Nucl. Energy, Part C **1**, 190 (1960).

[59]A. V. Brantov, V. Y. Bychenkov, V. T. Tikhonchuk, and W. Rozmus, "Nonlocal electron transport in laser heated plasmas," Phys. Plasmas **5**, 2742–2753 (1998).

[60]V. Y. Bychenkov, W. Rozmus, A. V. Brantov, and V. T. Tikhonchuk, "Theory of filamentation instability and stimulated Brillouin scattering with nonlocal hydrodynamics," Phys. Plasmas **7**, 1511 (2000).

[61]R. L. Berger, E. J. Valeo, and S. Brunner, "The transition from thermally driven to ponderomotively driven stimulated Brillouin scattering and filamentation of light in plasma," Phys. Plasmas **12**, 062508 (2005).

[62]M. Casanova, "Convenient computational forms for the frequency and damping of electrostatic waves in an unmagnetized plasma," Laser Part. Beams **7**, 165–171 (1989).

[63]S. Ghosal and H. A. Rose, "Two-dimensional plasma flow past a laser beam," Phys. Plasmas **4**, 2376–2396 (1997).

[64]S. Ghosal and H. A. Rose, "Effect of induced spatial incoherence on flow induced laser beam deflection: Analytic theory," Phys. Plasmas **4**, 4189–4191 (1997).

[65]H. A. Rose and S. Ghosal, "Effect of smoothing by spectral dispersion on flow induced laser beam deflection: The random phase modulation scheme," Phys. Plasmas **5**, 775–781 (1998).

[66]F. Gilleron and R. Piron, "The fast non-LTE code DEDALE," High Energy Density Phys. **17**, 219–230 (2015).

[67]H. Jourdren, "HERA: A hydrodynamic AMR platform for multi-physics simulations," in *Adaptive Mesh Refinement—Theory and Applications*, edited by

T. Plewa, T. Linde, and V. Gregory Weirs (Springer, Berlin, Heidelberg, 2005), pp. 283–294.

[68] R. L. Berger, C. H. Still, E. A. Williams, and A. B. Langdon, "On the dominant and subdominant behavior of stimulated Raman and Brillouin scattering driven by nonuniform laser beams," Phys. Plasmas **5**, 4337–4356 (1998).

[69] P. E. Masson-Laborde, S. Hüller, D. Pesme, M. Casanova, P. Loiseau, and C. Labaune, "Modeling parametric scattering instabilities in large-scale expanding plasmas," J. Phys. IV **133**, 247–251 (2006).

[70] A. V. Maximov, I. G. Ourdev, D. Pesme, W. Rozmus, V. T. Tikhonchuk, and C. E. Capjack, "Plasma induced smoothing of a spatially incoherent laser beam and reduction of backward stimulated Brillouin scattering," Phys. Plasmas **8**, 1319–1328 (2001).

[71] L. Videau, C. Rouyer, J. Garnier, and A. Migus, "Motion of hot spots in smoothed beams," J. Opt. Soc. Am. A **16**, 1672 (1999).

[72] C. J. Keane, National Ignition Facility User Guide, 2014.

[73] D. Penninckx, H. Coïc, A. Leblanc, A. Chatagnier, A. Bourgeade, E. d'Humières, and P. Loiseau, "Impact of FM-AM conversion on smoothing by spectral dispersion," Proc. SPIE **9345**, 93450P (2015).

[74] C. Huang, X. Lu, Y. Jiang, X. Wang, Z. Qiao, and W. Fan, "Real-time characterization of FM-AM modulation in a high-power laser facility using an RF-photonics system and a denoising algorithm," Appl. Opt. **56**, 1610–1615 (2017).

[75] M. Grech, "Modifications des propriétés de cohérence des faisceaux laser dans les plasmas de fusion par confinement inertiel," Ph.D. thesis, Université Bordeaux I, école doctorale des sciences physiques et de l'ingénieur, 2007.

[76] A. Le Cain, G. Riazuelo, and J. M. Sajer, "Statistical spatio-temporal properties of the laser megajoule speckle," Phys. Plasmas **19**, 102704 (2012).

[77] N. Lemos, W. A. Farmer, N. Izumi, H. Chen, E. Kur, A. Pak, B. B. Pollock, J. D. Moody, J. S. Ross, D. E. Hinkel, O. S. Jones, T. Chapman, N. B. Meezan, P. A. Michel, and O. L. Landen, "Specular reflections ('glint') of the inner beams in a gas-filled cylindrical hohlraum," Phys. Plasmas **29**, 092704 (2022).

[78] H. Honda, H. Nishimura, S. Miyamoto, D. Ohnuki, K. Fujita, Y. Ochi, H. Miki, H. Takabe, S. Nakai, and K. Mima, "Influence of specularly reflected laser light on uniformity of implosion of indirect-drive fusion capsule," Plasma Phys. Controlled Fusion **40**, 1097–1104 (1998).

[79] D. Turnbull, P. Michel, J. E. Ralph, L. Divol, J. S. Ross, L. F. Berzak Hopkins, A. L. Kritcher, D. E. Hinkel, and J. D. Moody, "Multibeam seeded Brillouin sidescatter in inertial confinement fusion experiments," Phys. Rev. Lett. **114**, 125001 (2015).

[80] A. L. Kritcher, D. Clark, S. Haan, S. A. Yi, A. B. Zylstra, D. A. Callahan, D. E. Hinkel, L. F. Berzak Hopkins, O. A. Hurricane, O. L. Landen, S. A. MacLaren, N. B. Meezan, P. K. Patel, J. Ralph, C. A. Thomas, R. Town, and M. J. Edwards, "Comparison of plastic, high density carbon, and beryllium as indirect drive NIF ablators," Phys. Plasmas **25**, 056309 (2018).

[81] M. Vandenboomgaerde, A. Grisollet, M. Bonnefille, J. Clérouin, P. Arnault, N. Desbiens, and L. Videau, "Hollow wall to stabilize and enhance ignition hohlraums," Phys. Plasmas **25**, 012713 (2018).

[82] S. Depierreux, V. Tassin, D. Antigny, R. E. Bahr, N. Botrel, R. Bourdenet, G. DeDemo, L. DeLaval, O. Dubos, J. Fariaut, M. Ferri, T. Filkins, S. LeTacon, C. Sorce, B. Villette, and M. Vandenboomgaerde, "Experimental evidence of harnessed expansion of a high-Z plasma using the hollow wall design for indirect drive inertial confinement fusion," Phys. Rev. Lett. **125**, 255002 (2020).

[83] V. Yahia, P.-E. Masson-Laborde, S. Depierreux, C. Goyon, G. Loisel, C. Baccou, N. G. Borisenko, A. Orekhov, T. Rienecker, O. Rosmej, D. Teychenné, and C. Labaune, "Reduction of stimulated Brillouin backscattering with plasma beam smoothing," Phys. Plasmas **22**, 042707 (2015).

[84] D. Turnbull, J. Katz, D. E. Hinkel, P. Michel, T. Chapman, L. Divol, E. Kur, S. MacLaren, A. L. Milder, M. Rosen, A. Shvydky, G. B. Zimmerman, and D. H. Froula, "Beam spray thresholds in ICF-relevant plasmas," Phys. Rev. Lett. **129**, 025001 (2022).

[85] R. K. Follett, J. G. Shaw, J. F. Myatt, C. Dorrer, D. H. Froula, and J. P. Palastro, "Thresholds of absolute instabilities driven by a broadband laser," Phys. Plasmas **26**, 062111 (2019).

[86] H. H. Ma, X. F. Li, S. M. Weng, S. H. Yew, S. Kawata, P. Gibbon, Z. M. Sheng, and J. Zhang, "Mitigating parametric instabilities in plasmas by sunlight-like lasers," Matter Radiat. Extremes **6**, 055902 (2021).

[87] A. Fusaro, P. Loiseau, D. Penninckx, G. Riazuelo, and R. Collin, "Improving stimulated Brillouin scattering mitigation in weakly-damped plasmas: From spectral dispersion to spectral distribution," Nucl. Fusion **61**, 126049 (2021).

[88] P. Michel, C. Labaune, S. Weber, V. T. Tikhonchuk, G. Bonnaud, G. Riazuelo, and F. Walraet, "Studies of the laser filament instability in a semicollisional plasma," Phys. Plasmas **10**, 3545–3553 (2003).

[89] F. Walraet, G. Riazuelo, and G. Bonnaud, "Propagation in a plasma of a laser beam smoothed by longitudinal spectral dispersion," Phys. Plasmas **10**, 811 (2003).